Supporting Information

A 2D donor-acceptor covalent organic framework with charge transfer for supercapacitors

Tao Li,‡[a] Xiaodong Yan,‡[a] Wen-Da Zhang,[a] Wang-Kang Han,[a] Yong Liu,[a] Yunxing Li,[a] Haiyan Zhu,[a] Zaijun Li,[a] and Zhi-Guo Gu*[ab]

[a]Key Laboratory of Synthetic and Biological Colloids, Ministry of Education, School of

Chemical and Material Engineering, Jiangnan University, Wuxi 214122, China

E-mail: zhiguogu@jiangnan.edu.cn

[b]International Joint Research Center for Photoresponsive Molecules and Materials, School of

Chemical and Material Engineering, Jiangnan University, Wuxi 214122, China

‡ These authors contributed equally to this work.

Table of Contents

Section S1. Synthesis

**Synthesis of tetraformyl-tetrathiafulvalene (TTF-fo)**

TTF-fo was synthesized according to the reported procedures with slight modification.[1] Firstly, 4,4-diethoxybut-2-ynal (10.39 g, 67 mmol), ethylenetrithiocarbonate (8.30 g, 61 mmol) and xylene (60 mL) were added into a 100 mL flask under N_2 atmosphere. The reaction mixture was heated to reflux at 156 °C for 10 h. After evaporation, SiO_2 filtration and recrystallization, yellow needles I were obtained. Secondly, ethanol solution (100 mL) of I (5 g, 18.9 mmol) was added dropwise into 20 mL ethanol solution including triethylorthoformate (3.1 g, 20.8 mmol) and PTSA (300 mg). The reaction mixture was heated to reflux at 84 °C for 3 h. After cooling, the solution was diluted with CH_2Cl_2, washed, dried and recrystallized to obtain yellow needles II. Thirdly, II (0.4 g, 1.18 mmol) and trimethyphosphite (15 mL) were added into a 50 mL flask. The reaction mixture was heated to reflux at 80 °C for 3 h. After evaporation, SiO_2 filtration and recrystallization, orange needles III were obtained. Finally, CH_2Cl_2 solution (20 mL) of III (0.594 g, 1.12 mmol) was treated by 40 mL of formic acid. The deep blue solid TTF-fo was collected. ^{1}H NMR (400 MHz, DMSO-d_6): δ 10.30 (s, CHO); ^{13}C NMR (DMSO-d_6) 108.47 (= CS_2), 149.41 (=C-CHO), 182.71 (CHO); $C_{10}H_4O_4S_4$, M^+ ·Calcd. 318.3. (Fig. S1-S3).

Synthesis of TTF-COF1
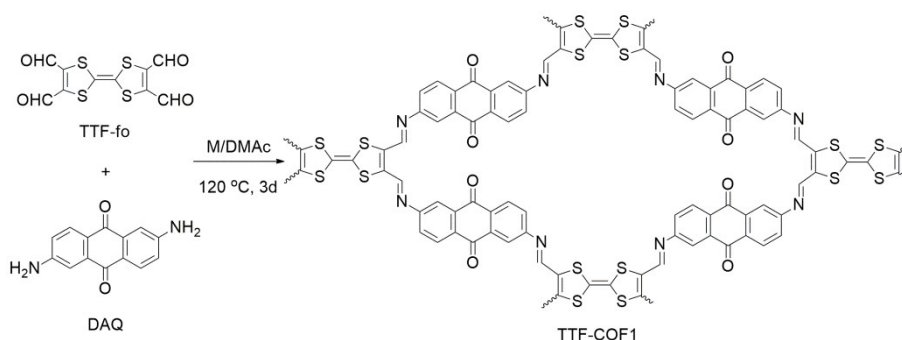
A glass bottle was charged with TTF-fo (15 mg, 0.047 mmol), DAQ (22.6 mg, 0.094 mmol), 1.75 mL of 1,2,3-trimethylbenzene (M) and 0.25 mL of dimethylacetamide (DMAc). The resulting solution was sonicated for 2 minutes to afford a homogenous dispersion, and then added with 0.2 mL of 3 M aqueous acetic acid. The glass bottle was transferred into a 25 mL Teflon-lined stainless steel autoclave. The autoclave was sealed and heated at 120 °C for 3 days and cooled to room temperature. The resulting black precipitate was collected by filtration and washed with THF (3 × 20 mL), DMF (3 × 20 mL) and MeOH (3 × 20 mL), Soxhlet extracted by THF 24 h (Caution! THF can produce peroxides that are potentially explosive and should be handled in small quantities with care!), then dried at 80 °C under vacuum for 24 h to give a black powder with 75% yield. Anal. Calcd. for $(C_{35}H_{20}N_2O_4S_2)_n$: C, 70.45; H, 3.38; N, 4.69; O, 10.73; S, 10.75. Found C, 70.31; H, 3.53; N, 4.62; O, 10.87; S, 10.67. FT-IR (power, cm^{-1}): 3382, 1706, 1659, 1628, 1585, 1538, 1445, 1332, 1299, 1158, 1078, 978, 891, 844, 751, 663, 576.

Synthesis of TTF-COF2
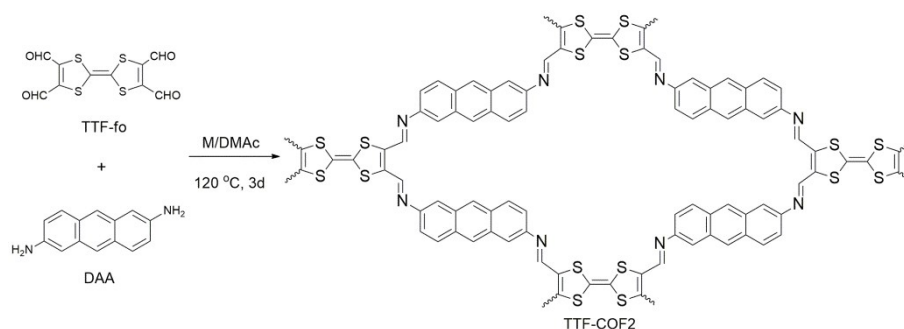
A glass bottle was charged with TTF-fo (15 mg, 0.047 mmol), DAA (19.8 mg, 0.094 mmol), 1.75 mL of M and 0.25 mL of DMAc. The resulting solution was sonicated for 2 minutes to afford a homogenous dispersion, and then added 0.2 mL of 3 M aqueous acetic acid. The glass bottle was transferred into a 25 mL Teflon-lined stainless steel autoclave. The autoclave was sealed and heated at 120 °C for 3 days and cooled to room temperature. The resulting brown precipitate was collected by filtration and washed with THF (3 × 20 mL), DMF (3 × 20 mL) and MeOH (3 × 20 mL), Soxhlet extracted by THF 24 h (Caution! THF can produce peroxides that are potentially explosive and should be handled in small quantities with care!), then dried at 80 °C under vacuum for 24 h to give a brown powder with 72% yield. Anal. Calcd. for $(C_{12}H_8NS_2)_n$: C, 62.58; H, 3.50; N, 6.08; S, 27.84. Found C, 62.43; H, 3.88; N, 6.01; S, 27.68. FT-IR (power, cm^{-1}): 3347, 1677, 1620, 1576, 1473, 1370, 1306, 1283, 1129, 1042, 962, 888, 802, 729, 668, 595.

Section S2. Materials Characterization: Fourier transform infrared (FT-IR) spectra were recorded on a Thermo Nicolet iS10 spectrometer in the spectral range of 500-4000 cm^{-1}. Polarized infrared reflection spectra were conducted by FT-IR spectrometer (Nicolet, Magna560) equipped with a microscope. UV-Vis diffuse reflectance spectrum (Kubelka-Munk spectrum) was collected using a JASCO model V-670 spectrometer equipped with integration sphere model IJN-727. ^{1}H NMR spectra were collected on a MERCURY plus 400 spectrometer. ^{13}C cross-polarization with magic angle-spinning (CP-MAS) solid-state nuclear magnetic resonance (NMR) spectra were recorded on a Bruker ARX 300 MHz spectrometer. X-ray photoelectron spectroscopy (XPS) analysis was conducted by a Thermo Scientific ESCALAB 250 XI. Thermogravimetric analyses (TGA) were taken using a Mettler Toledo TGA/DSC1/1100SF analyser in the temperature range of 50 to 800 °C under flowing N_2. Powder X-ray diffraction (PXRD) patterns were obtained from a Bruker D8 diffractometer using *Cu Kα* (λ = 1.54059 Å) radiation. The Brunauer-Emmett-Teller (BET) surface areas were collected on N_2 sorption isotherms at 77 K using a Micromeritics ASAP2020 surface area and pore size analyser. Pore size distribution was determined by nonlocal density functional theory mode in the instrument software package. Scanning electron microscopy (SEM) images were obtained on a Hitachi S-4800. Transmission electron microscopy (TEM) images were collected on a JEOL JEM-2100. Scanning transmission electron microscopy (STEM) images, HRTEM images and EDS mapping were carried out on a Tecnai G2 F30 transmission electron microscopy at an acceleration voltage of 300 kV.

Section S3. Electrochemical Characterization: The electrochemical performances of the samples were studied on an electrochemical station (CHI760E). Cyclic voltammetry (CV), galvanostatic charge-discharge (GCD) and electrochemical impedance spectroscopy (EIS) tests were conducted on in a three-electrode setup, including a Pt plate (1 cm^2) as the counter electrode and Hg/HgO electrode as the reference electrode. The active material, acetylene black and poly(tetrafluoethylene) in a mass ratio of 80:15:5 were mixed, and then dispersed in ethanol by ultrasonication to obtain homogeneous slurry. The slurry was coated on a Ni foam substrate (1 cm^2). The mass loading of the active materials on Ni foam was 5.0 mg cm^{-2}. Moreover, the asymmetric supercapacitors were assembled to test the electrochemical performance, with activated materials acting as the positive electrode and activated carbon (AC) as the negative electrode. The mass ratio of the positive and negative electrodes should be $m^+/m^- = (C^- \times \Delta V^-)/(C^+ \times \Delta V^+) = (184 \times 1)/(752 \times 0.5) \approx 1:2$. All the electrochemical measurements were performed in 3 M KOH aqueous electrolyte. EIS measurements were performed by in the frequency range from 0.01 to 10^5 Hz at open circuit potential with a potential amplitude of 5 mV.

Section S4. Calculation Section

The specific capacitance of electrode materials was calculated by the following equations:[2]

$$E_{\text{int}/D} = I \int_{t(U_{\max})}^{t(U_{\min})} U(t)dt \tag{1}$$

$$C_{\text{int}/D} = \frac{2E_{\text{int}/D}}{U_{\max}^2} \tag{2}$$

where $E_{int/D}$ is the energy density (Wh kg^{-1}), I is the discharge current, U is the potential range (V), t is the discharge time (s), $C_{int/D}$ is the specific capacitance (F g^{-1}).

Energy density and power density of the **TTF-COF1** are evaluated according to equation (3) and equation (4), respectively:

$$E = \frac{1}{2}C_{sp}V^2 \tag{3}$$

$$P = \frac{E}{\Delta t} \tag{4}$$

where E stands for the energy density (Wh kg^{-1}), C_{sp} represents the specific capacitance (F g^{-1}), V refers to the potential window (V), P is the power density (W kg^{-1}) and Δt is the discharge time (S).

Section 5. Supplementary data
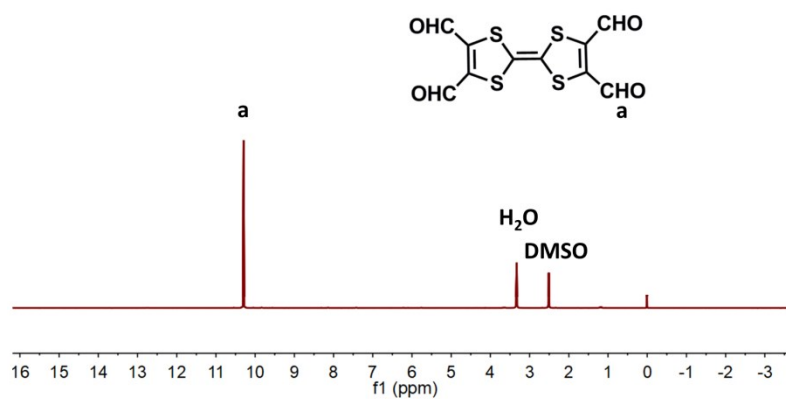
Fig. S1 ^{1}H-NMR spectrum of TTF-fo.
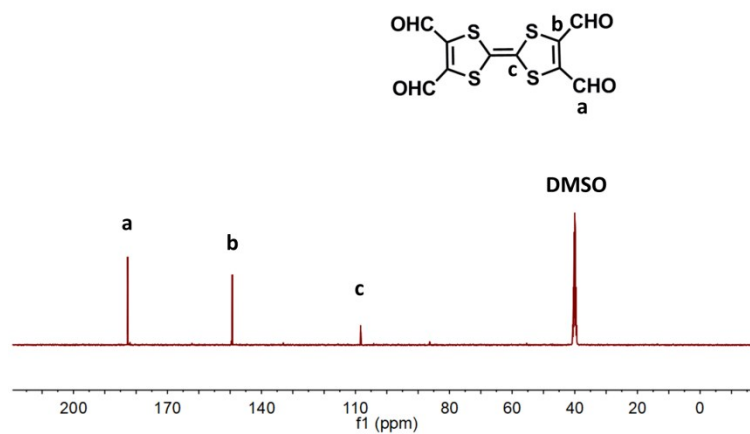
Fig. S2 ^{13}C-NMR spectrum of TTF-fo.
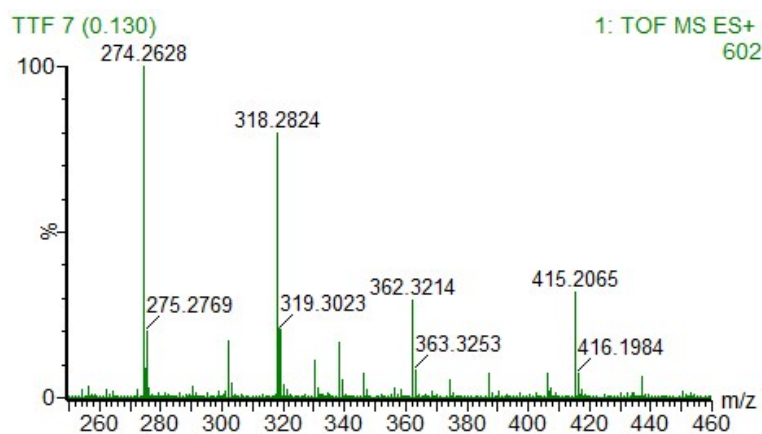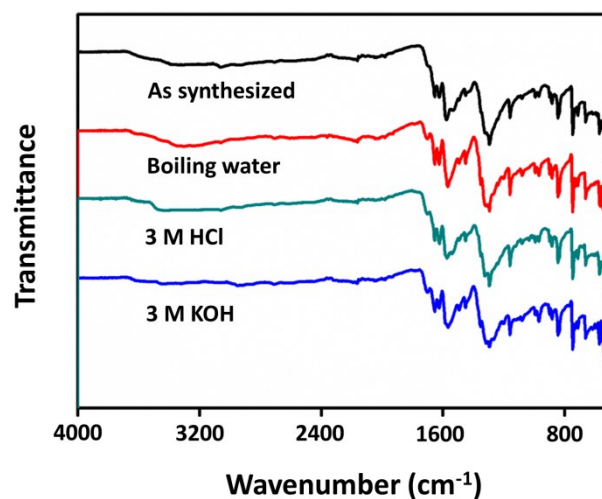

Fig. S3 Mass spectrometry of TTF-fo.

Fig. S4 Chemical stability test of **TTF-COF1**: the FT-IR patterns of **TTF-COF1** treated for 5 days in different solvents.
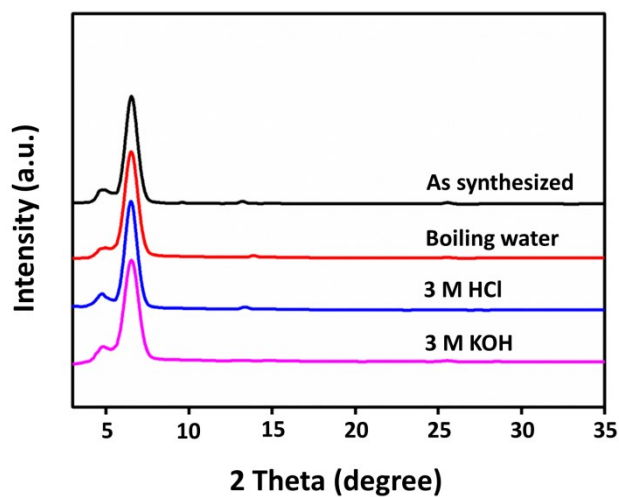

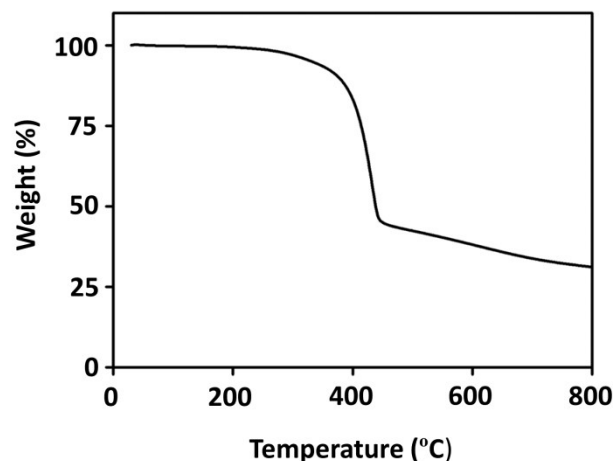**Fig. S5** Chemical stability test of **TTF-COF1**: the PXRD patterns of **TTF-COF1** treated for 5 days in different solvents.

Fig. S6 Thermogravimetric analysis (TGA) curve of **TTF-COF1**.

The weight of the **TTF-COF1** exhibited no discernible change below 300 °C. **TTF-COF1** started to decompose at 300 °C, and there was still 30% of weight residual for **TTF-COF1** at 800 °C. These indicated its excellent thermal stability.
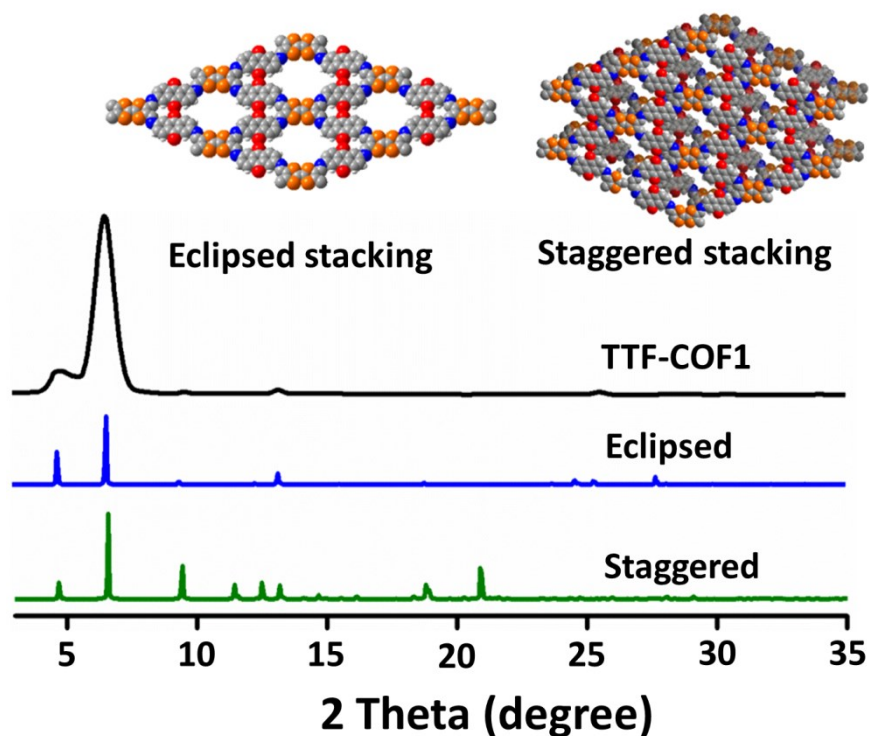
Fig. S7 PXRD patterns of **TTF-COF1** collected experimentally (black) and calculated with the eclipsed (blue) and staggered (green) stacking models. Comparison of the experimental and the simulated PXRD profiles indicated that the preferable structure of **TTF-COF1** is the eclipsed arrangement.

S10
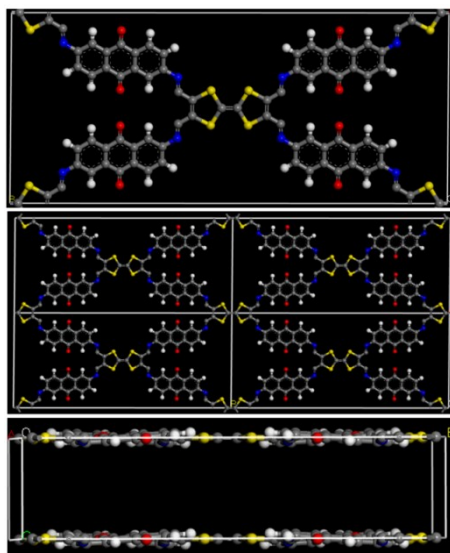
Fig. S8 Simulation of the **TTF-COF1** unit cell.

Simulation of the **TTF-COF1** unit cell content calculated in a slip-AA arrangement (along the y-axis): top view onto the ab-plane and view perpendicular to the b-axis. The simulation obviously elucidates the 2D structure with monoclinic C2/m space group and eclipsed stacking model. **TTF-COF1** connected by TTF units with rhombus pores, and the layer-by-layer stacking was also observed.
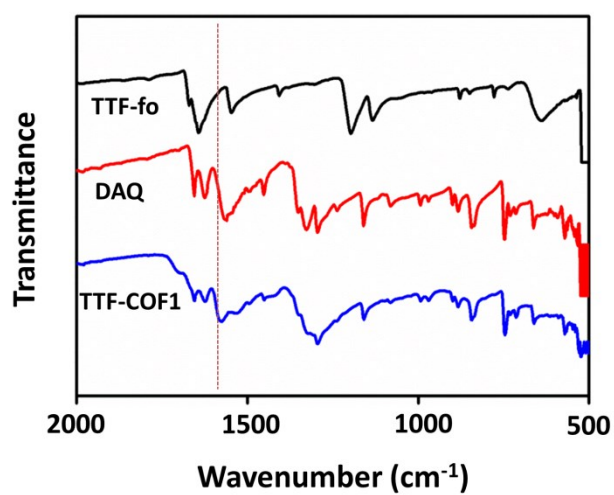

Fig. S9 Magnified FT-IR spectra region of TTF-fo, DAQ and **TTF-COF1**.
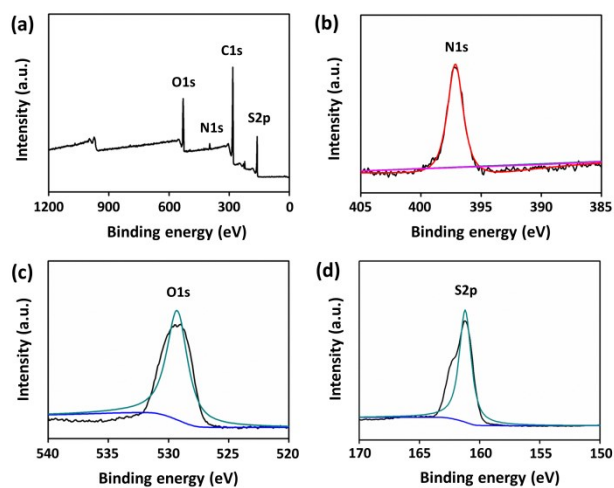
Fig. S10 XPS measurements of **TTF-COF1**: (a) survey, (b) N 1s, (c) O 1s and (d) S 2p spectra.

The N 1s peak at 397 eV, O 1s peak at 529.4 eV and S 2p peak at 161 eV are attributed to the C=N, C=O and C-S bonds, respectively.
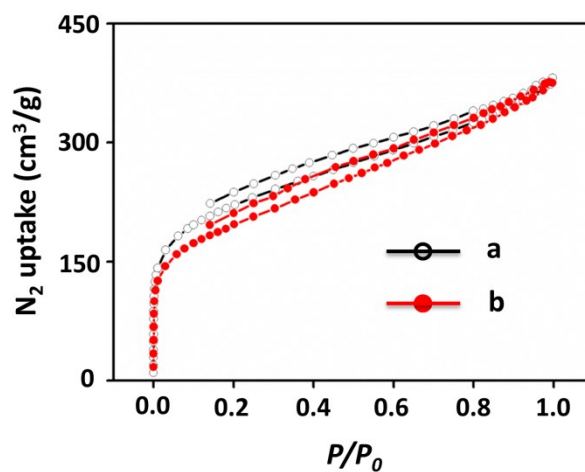

Fig. S11 Nitrogen adsorption-desorption isotherm of **TTF-COF1** (a) Before and (b) after immersing in acids, bases, boiling water and organic solvents.
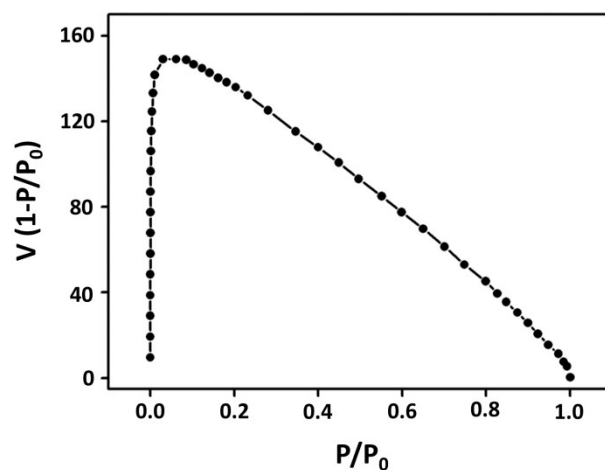
Fig. S12 Calculated Rouquerol plot of **TTF-COF1** along with pressure ranges used for the BET surface area calculations.
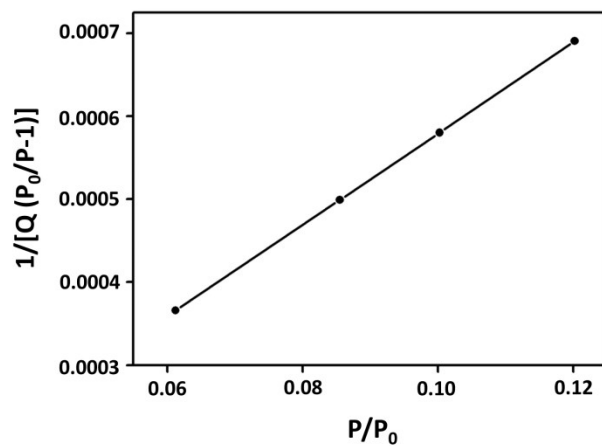

Fig. S13 BET plots of **TTF-COF1** from nitrogen isotherms at 77 K. The selected points are located in the relative pressure ranges (between 0.01 and 0.12). Correlation coefficient R was 0.9999. The values of BET slope and BET intercept is 0.00563 and 0.000328, respectively.
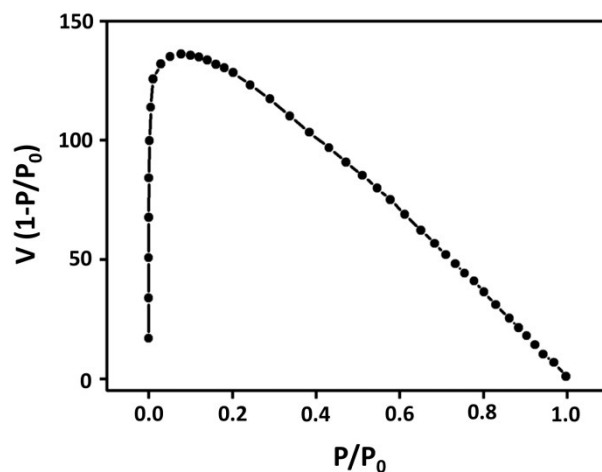
Fig. S14 Calculated Rouquerol plot of **TTF-COF1** after immersing in acids, bases, boiling water and organic solvents.
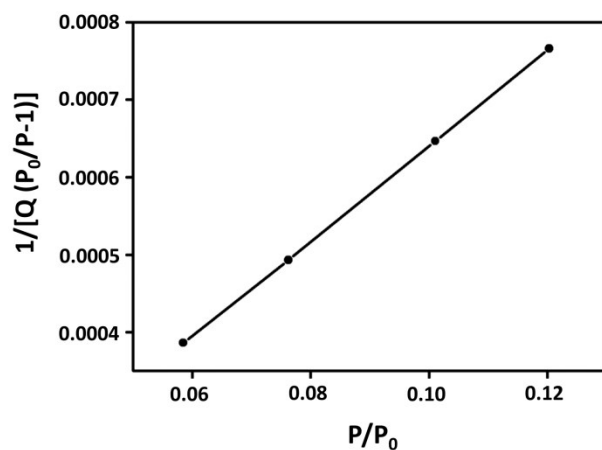

Fig. S15 BET plots of **TTF-COF1** after immersing in acids, bases, boiling water and organic solvents. The selected points are located in the relative pressure ranges (between 0.01 and 0.12). Correlation coefficient R was 0.9999. The values of BET slope and BET intercept is 0.00603 and 0.000334, respectively.
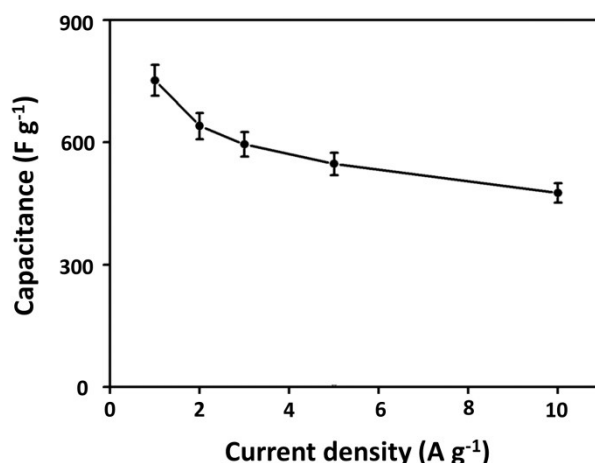
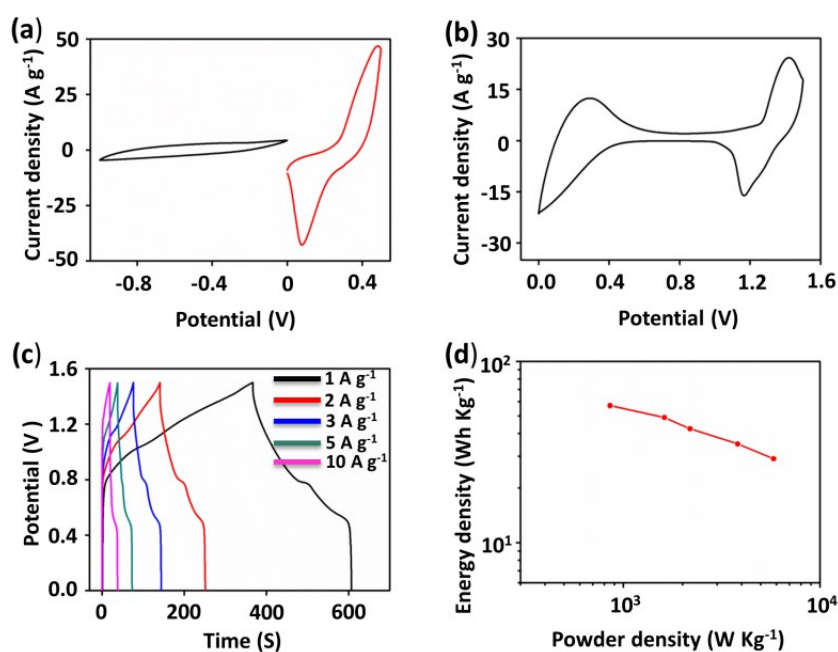**Fig. S16** Error bars of capacitance vs. current density for **TTF-COF1**.

Fig. S17 (a) CV curves of the AC electrode and **TTF-COF1** electrode at a scan rate of 100 mV s^{-1} in a three-electrode system. (b) CV curve of assymetric supercapacitor at a scan rate of 100 mV s^{-1}. (c) GCD curves of assymetric supercapacitor at different current densities. (d) Energy density of the assymetric supercapacitor.

The AC (-1.0-0 V) and **TTF-COF1** (0-0.5 V) offer different potential ranges, and their combination can obviously extend the potential range, which is benefit for improving the energy density of supercapacitors. The CV curves of the asymmetric supercapacitor exhibited a pair of redox peaks in the potential range of 0-1.5 V. The specific capacitance of the asymmetric supercapacitor was calculated to be 183, 157, 136, 112 and 93 F g^{-1} in the range from 1 to 10 A g^{-1}, respectively. The energy density reaches 57 Wh kg^{-1} at a power density of 858 W kg^{-1}. The energy density is still as high as 29 Wh kg^{-1} even at 5813 W kg^{-1}.
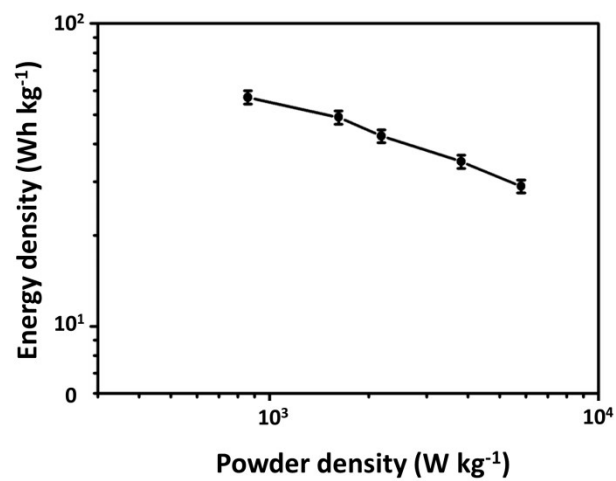
Fig. S18 Error bars of energy density vs. powder density for **TTF-COF1**.
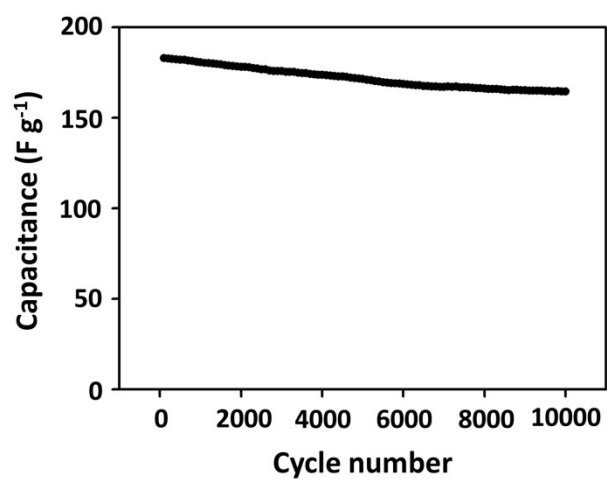

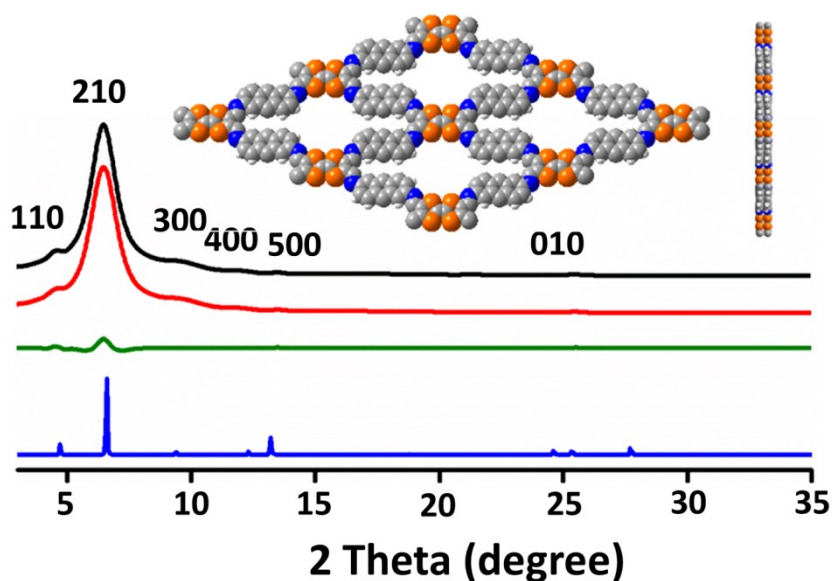**Fig. S19** Cyclic stability of AC//**TTF-COF1**.

Fig. 20 PXRD patterns of **TTF-COF2** with the experimental profiles in black, Pawley-refined profiles in red, calculated profiles in blue, and the differences between the experimental and refined PXRD patterns in green (the inserts exhibit simulated structure with a 2D eclipsed layered arrangement).
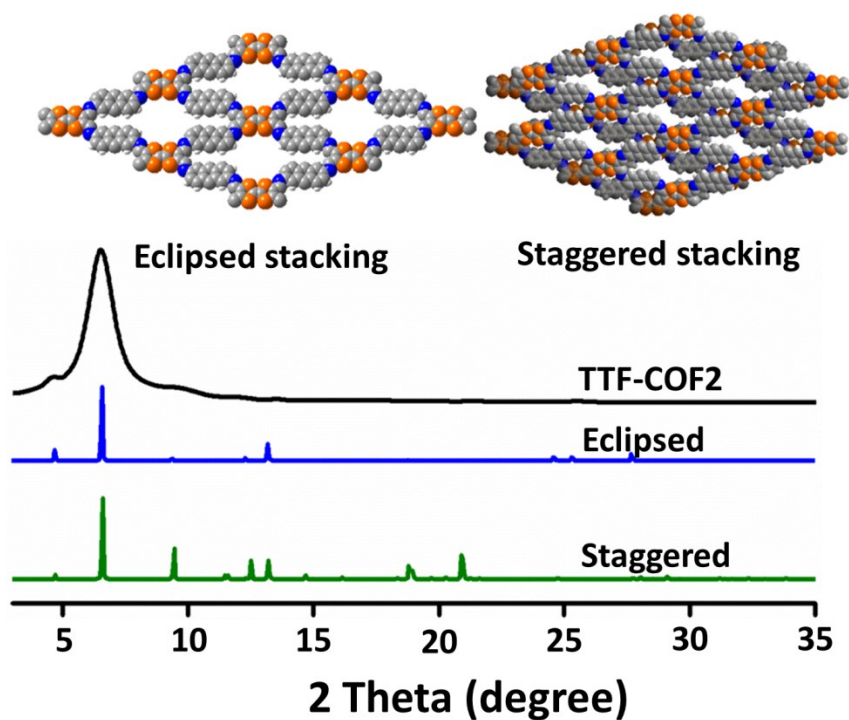

Fig. S21 PXRD patterns of **TTF-COF2** observed (black) and calculated with the eclipsed (blue) and staggered (green) stacking models. Comparison of the observed and the simulated PXRD profiles indicated that the preferable structure of **TTF-COF2** is the eclipsed arrangement.
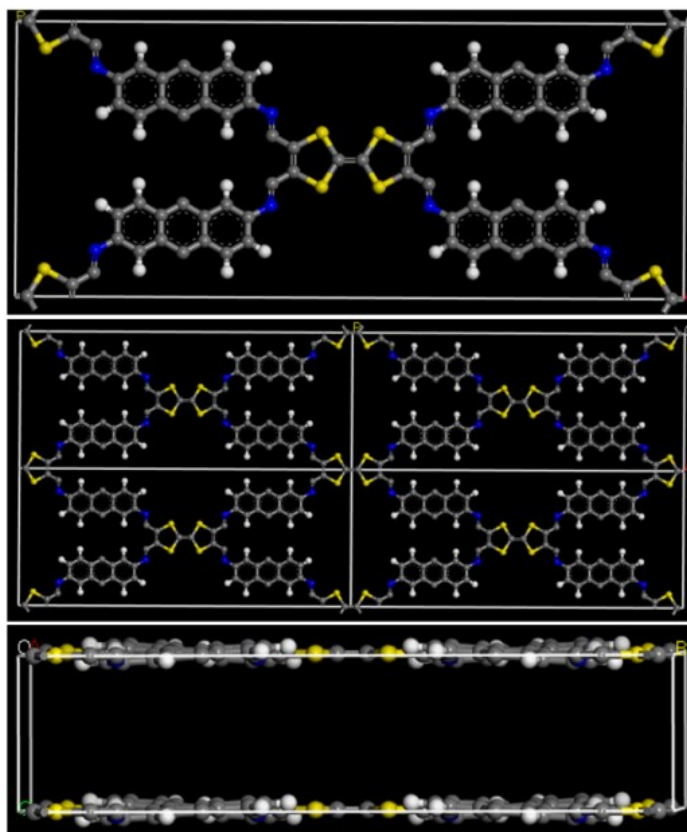
Fig. S22 Simulation of the **TTF-COF2** unit cell.

Simulation of the **TTF-COF2** unit cell content calculated in a slip-AA arrangement (along the y-axis): top view onto the ab-plane and view perpendicular to the b-axis. The simulation obviously elucidates the 2D structure with monoclinic C2/m space group and eclipsed stacking model. **TTF-COF2** connected by TTF units with rhombus pores, and the layer-by-layer stacking was also observed.
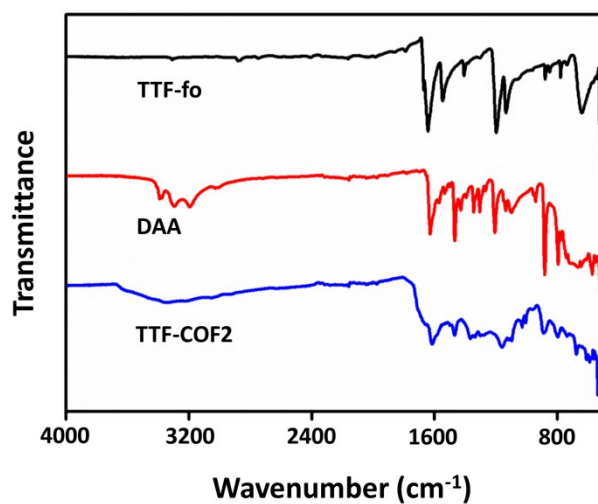
Fig. S23 FT-IR spectra of TTF-fo, DAA and **TTF-COF2**.

The disappearance of the characteristic C=O vibration band (1652 cm^{-1}) and N-H vibration band (3193-3397 cm^{-1}), and the appearance of C=N bonding (1620 cm^{-1}), indicates the formation of **TTF-COF2**.
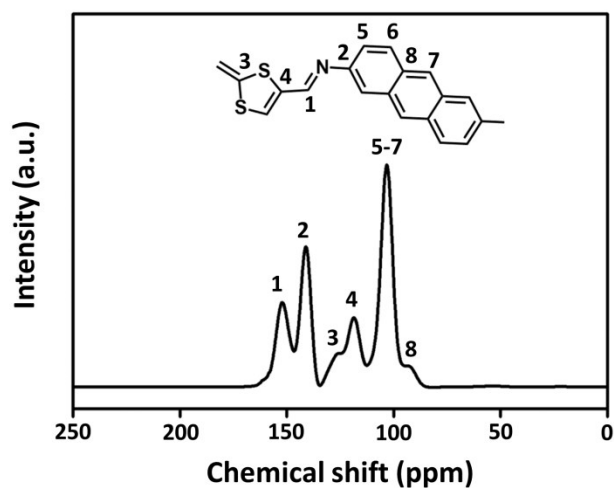

Fig. S24 ^{13}C-CP-MAS solid-state NMR spectrum of **TTF-COF2**.

The characteristic resonance signal at 154 ppm is derived from the C=N group, which clearly reveals the formation of **TTF-COF2**.

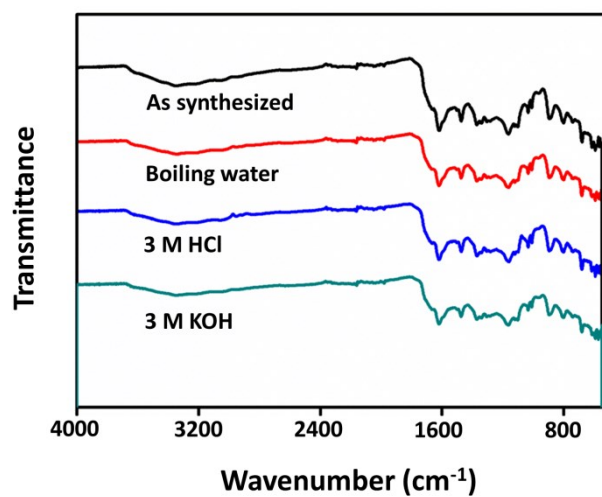**Fig. S25** Chemical stability test of **TTF-COF2**. The FT-IR patterns of **TTF-COF2** treated for 5 days in different solvents.
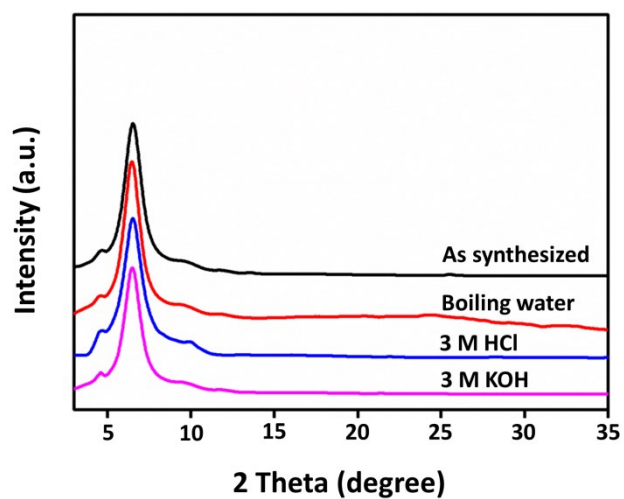

Fig. S26 Chemical stability test of **TTF-COF2**. The PXRD patterns of **TTF-COF2** treated for 5 days in different solvents.
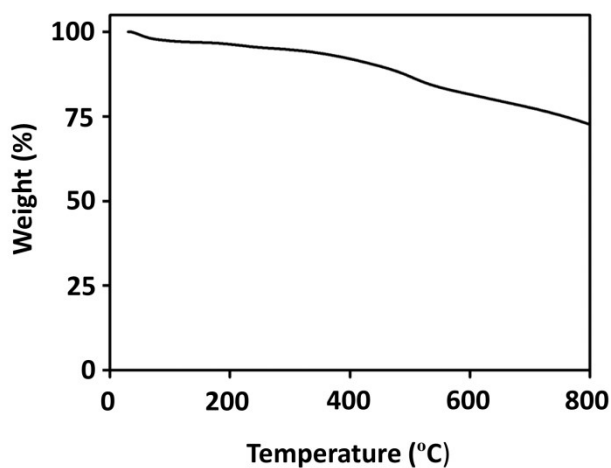
Fig. S27 Thermogravimetric analysis (TGA) curve of **TTF-COF2**.

The weight of the **TTF-COF2** decreased slightly below 100 °C, which could be attributed to the weight loss of solvent. **TTF-COF2** exhibited no discernible weight loss from 100 to 393 °C, and then **TTF-COF2** started to decompose. Further heated to 800 °C, there was still 72% of weight residual for **TTF-COF2**, indicating its excellent thermal stability.
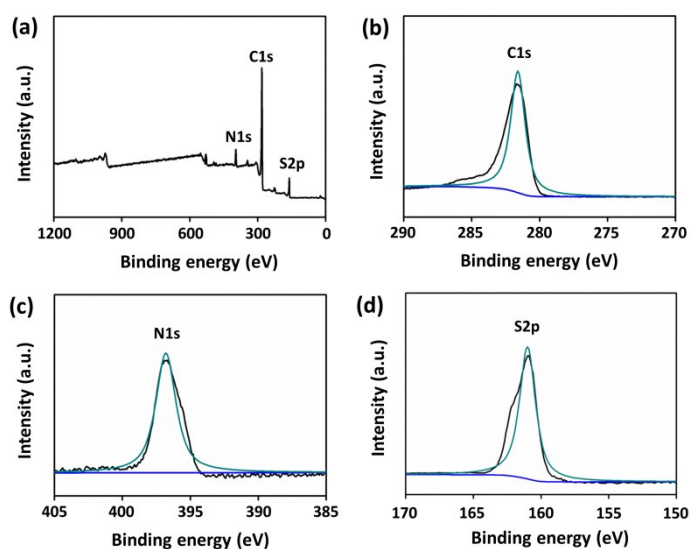
Fig. S28 XPS measurements of **TTF-COF2**: (a) survey, (b) C 1s, (c) N 1s and (d) S 2p spectra.

The N 1s peak at 397 eV and S 2p peak at 161 eV are attributed to the C=N and C-S bonds, respectively.
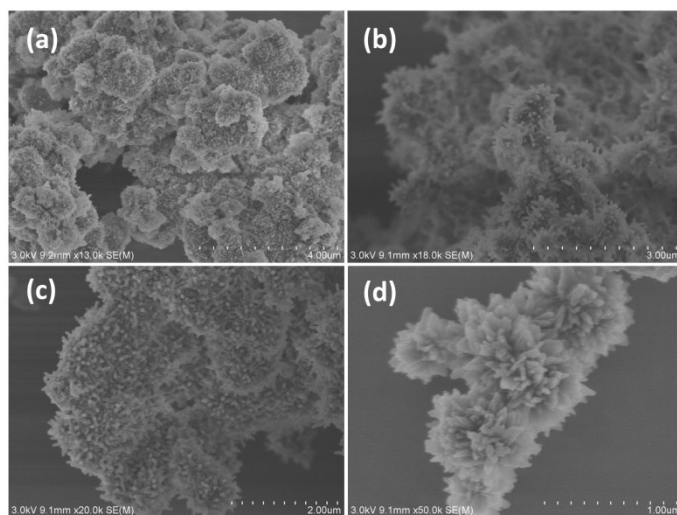
Fig. S29 SEM images of **TTF-COF2**.

TTF-COF2 exhibits a flower-like structure with dimension of 2 μm, composing of numerous tightly stacked rods.

Fig. S30 TEM images of **TTF-COF2**.

The TEM images clearly clarify that **TTF-COF2** exhibits orderly layer-by-layer and porous structure.
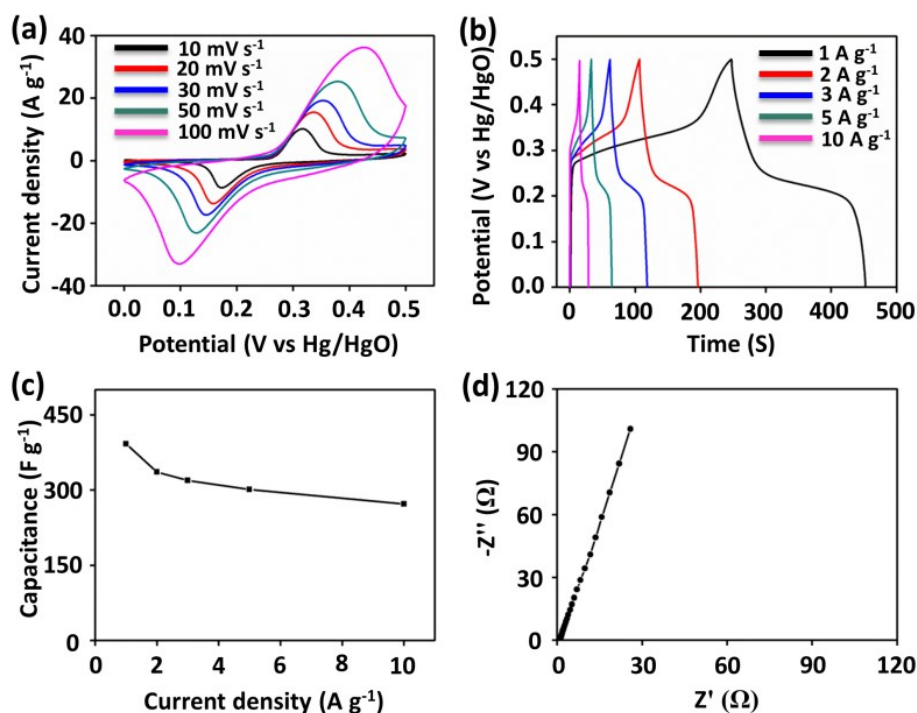
Fig. S31 Electrochemical measurement of **TTF-COF2** in a three-electrode system. (a) CV profiles at various scan rates (10-100 mV s^{-1}). (b) GCD curves at various current densities (1-10 A g^{-1}). (c) Capacitance at various current densities (1-10 A g^{-1}). (d) The Nyquist plot of **TTF-COF2**.
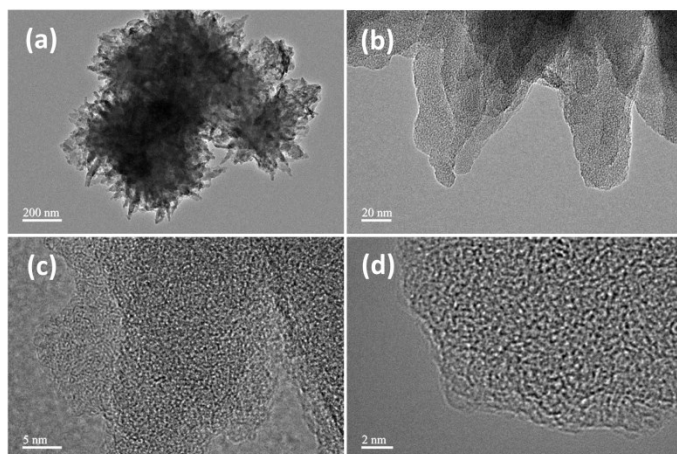
The CV curves collected at different scan rates from 10 to 100 mV s^{-1} display a pair of redox peaks, indicating the pseudocapacitive behaviour. The GCD curves exhibit a severely distorted triangular shape, which is resulted from the typical pseudocapacitive behaviour, in agreement with the CV analyses. The discharging capacitances of **TTF-COF2** are calculated to be 392, 336, 319, 301 and 272 F g^{-1} at 1, 2, 3, 5 and 10 A g^{-1}, respectively. The specific capacitance at 10 A g^{-1} retains 69% of that at 1 A g^{-1}, indicating its good rate capability. EIS test indicates low charge transfer resistance, which is favourable for good rate performance.
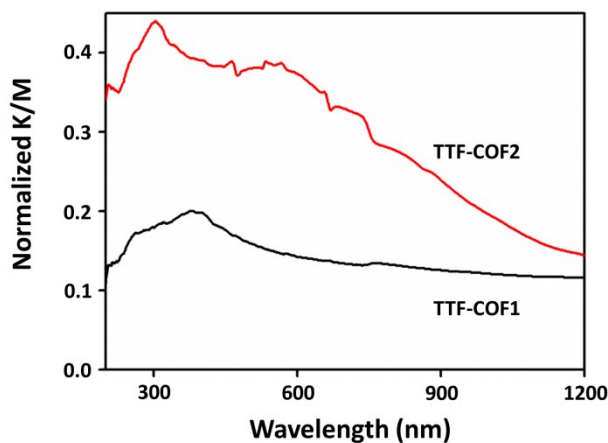
Fig. S32 UV-vis spectra of **TTF-COF1** and **TTF-COF2**.

Table S1 Comparison of specific capacitance with COFs electrode materials.

Electrode type	Electrolyte	Current density/scan rate	Specific capacitance ($F\ g^{-1}$)	References
DqTp-COF	1 M H_2SO_4	1.56 mA cm^{-2}	154	3
DAAQ-TFP-COF	0.5 M H_2SO_4	20 mV s^{-1}	197	4
DAAQ-TFP COF	1 M H_2SO_4	0.1 A g^{-1}	49	5
TpOMe-DAQ	3 M H_2SO_4	3.3 mA cm^{-2}	169	6
TaPa-Py-COF	1 M H_2SO_4	0.5 A g^{-1}	209	7
TpPa-$(OH)_2$	1 M Phosphate buffer	0.5 A g^{-1}	416	8

Table S2 Fractional atomic coordinates for the monoclinic C2/m unit cell of **TTF-COF1** calculated using the Materials Studio 7.0.

TTF-COF1			
monoclinic C2/m a = 16.500 (12) Å, b = 37.478 (16) Å, c = 3.692 (11) Å, β = 119.414° (14)			
A1	0.54462	-0.41484	1.02512
A2	0.39920	-0.45705	0.93080
A3	0.58820	-0.38284	1.03322
A4	0.30291	0.15266	0.13109
A5	0.21263	0.15248	0.07218
A6	0.16494	0.18506	1.00947
A7	0.20698	0.21761	1.00537
A8	0.29840	0.21743	0.06291
A9	0.34555	0.18468	0.12653
A10	0.15922	0.25019	0.94558
A11	0.08105	0.25038	0.90374
A12	0.34023	0.12779	0.17858
A13	0.09489	0.18505	0.96385
A14	0.41545	0.18370	0.17071
A15	0.67060	0.38104	0.07406
A16	1/2	-0.48203	1.00000

Table S3 Fractional atomic coordinates for the monoclinic C2/m unit cell of **TTF-COF2** calculated using the Materials Studio 7.0.

TTF-COF2			
monoclinic C2/m $a = 16.500 \ (12) \ \text{Å}, \ b = 37.478 \ (16) \ \text{Å}, \ c = 3.692 \ (11) \ \text{Å}, \ \beta = 119.414° \ (14)$			
A1	0.54462	-0.41484	1.02512
A2	0.39920	-0.45705	0.93080
A3	0.58820	-0.38284	1.03322
A4	0.30291	0.15266	0.13109
A5	0.21263	0.15248	0.07218
A6	0.16494	0.18506	1.00947
A7	0.20698	0.21761	1.00537
A8	0.29840	0.21743	0.06291
A9	0.34555	0.18468	0.12653
A10	0.15922	0.25019	0.94558
A11	0.34023	0.12779	0.17858
A12	0.09489	0.18505	0.96385
A13	0.41545	0.18370	0.17071
A14	0.67060	0.38104	0.07406
A15	1/2	-0.48203	1.00000

Section 6. References

1   M. Sallé, A. Gorgues, M. Jubault, K. Boubekeur, P. Batail, *Temhedron*, 1992, **48**, 3081-3090.

2   A. Laheäär, P. Przygocki, Q. Abbas, F. Béguin, *Electrochem. Commun.*, 2015, **60**, 21-25.

3   M. A. Khayum, V. Vijayakumar, S. Karak, S. Kandabeth, M. Bhadra, K. Suresh, N. Acharambath, S. Kurungot, R. Banerjee, ACS Appl. Mater. Interfaces, 2018, **10**, 28139-28146.

4   C. R. Mulzer, L. X. Shen, R. P. Bisbey, J. R. McKone, N. Zhang, H. D. Abruña, W. R. Dichtel, ACS Cent. Sci., 2016, 2, 667-673.

5   C. R. DeBlase, K. E. Silberstein, T. T. Truong, H. D. Abruña, W. R. Dichtel, J. Am. Chem. Soc., 2013, 135, 16821-16824.

6   A. Halder, M. Ghosh, M. A. Khayum, S. Bera, M. Addicoat, H. S. Sasmal, S. Karak, S. Kurungot, R. Banerhee, J. Am. Chem. Soc., 2018, 140, 10941-10945

7   A. M. Khattak, Z. A. Ghazi, B. Liang, N. A. Khan, A. Iqbal, L. S. Li, Z. Y. Tang, J. Mater. Chem. A, 2016, 4, 16312-16317.

8   S. Chandra, D. R. Chowdhury, M. Addicoat, T. Heine, A. Paul, R. Banerjee, Chem. Mater., 2017, 29, 2074-2080.